# Surface-tension effects in oscillatory squeeze flow rheometry

- J. M. Barakat, <sup>1, a)</sup> Z. Hinton, <sup>2</sup> N. J. Alvarez, <sup>2</sup> and T. W. Walker<sup>3</sup>
- <sup>1)</sup>Department of Chemical Engineering, University of California, Santa Barbara, California 93106, ISA
- <sup>2)</sup>Department of Chemical and Biological Engineering, Drexel University, Philadelphia, Pennsylvania 19104, USA
- <sup>3)</sup>Department of Chemical and Biological Engineering, South Dakota School of Mines and Technology, Rapid City, SD, 57701, USA

(Dated: 21 November 2021)

Oscillatory squeeze flow rheometry (OSFR) is a technique for measuring fluid viscosity and linear viscoelasticity between oscillating parallel plates. While several corrections to the basic viscous flow model for OSFR have been considered (e.g., due to inertial effects), the role of surface tension remains largely unexplored. The present work revisits the classical liquid bridge problem subject to an oscillatory squeeze flow and considers the role of viscosity and surface tension on the dynamic force exerted by the liquid on the supporting plates. Using a combination of theory and experiment, we show that the (dimensionless) force collapses onto a master curve when plotted against a modified capillary number (measuring the relative importance of viscosity and surface tension) and that this prediction is robust over wide range of strain amplitudes and aspect ratios. In doing so, we also demonstrate the ability of OSFR to measure surface-tension forces with reasonably high resolution. We test this capability for several low-viscosity fluids, demonstrating that, with current instrumentation and protocol, OSFR can measure surface tension to within 20% relative error. Finally, we provide an operating diagram that demarcates the regimes in which either viscosity or surface tension can be ignored in OSFR measurements. The results of this study may be used to further develop OSFR as a tool for measuring dynamical surface phenomena, in additional to bulk viscoelasticity.

#### I. INTRODUCTION

Squeeze flows frequently occur in engineering practice, as in compression molding and motor bearing lubrication, as well as in biological systems, most notably in the synovial fluid within the knee joint. Oscillatory squeeze flow rheometry (OSFR) has received recent attention as a method for probing the linear viscoelastic behavior of non-Newtonian fluids in inhomogeneous (mixed) flows. 1-5 The method involves placing a small sample of fluid (typically 10-100 microliters in volume) between two parallel plates; the top plate oscillates vertically along its axis while the stationary base plate measures the axial force exerted by the liquid. The newest implementation of OSFR uses a filament stretching rheometer (FSR), which enables simultaneous measurement of the radial deformation of the liquid bridge.<sup>6</sup> Whereas traditional FSR measurements are designed for nonlinear extensional rheology, an FSR used in OSFR mode can additionally extract the linear viscoelastic response of a liquid undergoing mixed squeeze flow.

In interpreting OSFR measurements, several factors including fluid inertia must be painstakingly taken into account<sup>2,7,8</sup> while others, including gravity and surface tension, are typically ignored.<sup>1</sup> The neglect of surface tension in OSFR is a valid assumption when the sample is sufficiently viscous (or viscoelastic) and the frequency of oscillation is high enough such that the force measured at the base plate can be attributed entirely to the deformation of the bulk fluid. However, in circumstances where *either* the frequency of oscillation or the viscosity of the fluid sample are not appreciably large, the

surface-tension force cannot be neglected – in some cases, it can even become the dominant effect. This raises the issue of modeling the nonlinear capillary response of a liquid bridge undergoing axial oscillation and de-convolving this response from the viscoelasticity of the bulk fluid.

Numerous studies have examined the role of surface tension in extensional rheometry (e.g., traditional FSR)<sup>9–14</sup> and shear rheometry. <sup>15–18</sup> Capillary effects in *static* liquid bridges are well established <sup>19–34</sup> and relate to the force of adhesion between two substrates. <sup>35</sup> Pitois, Moucheront, and Chateau <sup>36</sup> extended these static analyses by considering the influence of viscosity on the dynamic, albeit *steady*, force of adhesion between two substrates separating at constant velocity.

By comparison, the literature on oscillating liquid bridges is relatively sparse, and very few studies have considered capillary effects in OSFR. Anna and McKinley <sup>37</sup> considered the influence of an oscillatory pre-squeezing flow on extensional FSR measurements, but neglected surface tension in their analysis. Montanero and coworkers<sup>31,38–41</sup> have published several studies investigating the surface tension and shape dynamics of liquid bridges in oscillation, including the effect of surfactants<sup>42,43</sup> and surface shear viscosity.<sup>44</sup> However, in these studies the force exerted on the base plate was not reported, precluding a direct application to OSFR measurements. Valsamis and coworkers<sup>45</sup> modeled an oscillating liquid bridge as a spring-dashpot system (a Kelvin-Voigt arrangement) in order to extract "effective" material properties from experiments and simulations. Unfortunately, the results from their experiments, as well as the model used for the surface-tension force, are not particularly easy to interpret. In particular, it is not obvious how the measured force depends on experimentally controlled parameters such as the volume of the fluid sample or the amplitude and frequency of oscillation. This is the focus of the present study.

a) Electronic mail: josephbarakat@ucsb.edu

There are two principal reasons for which one would care to quantify surface-tension effects in OSFR. Firstly, surface tension can emerge as an unwanted artifact in measurements of viscometric functions for fluids of low to moderate viscosity. Naturally, one might expect this "contamination by surface tension" to be minimized for large values of the capillary number  $\text{Ca} = \mu \omega R_0/\gamma$ , where  $\mu$  is the Newtonian or zeroshear-rate viscosity,  $\omega$  is the angular frequency,  $R_0$  is the radius of the top and bottom plate, and  $\gamma$  is the surface tension. However, this criterion  $\text{Ca} \gg 1$  does not elucidate the sensitivity of the surface-tension force to the height of the bridge or the applied axial strain, both of which are expected to have a significant effect.

A second reason would be to use OSFR to measure surface tension and, more generally, the dynamical surface properties of fluids. In this application, OSFR could become a technique similar to the oscillating bubble method, with the novel advantage of using a cylindrical geometry instead of a spherical one. Pertinent applications of such a technique include the measurement of the stiffness of surface-oxide layers in liquid metals<sup>46</sup> as well as the kinetics of surfactant adsorption onto a cylindrical liquid column.<sup>47</sup>

Rather than focus on complicated systems such as these, however, our aim in the present study is to quantify the effect of surface tension for oscillating bridges of simple, Newtonian liquids with constant surface tension. Our motivation is to determine an operating space in which surface-tension effects can either be ignored entirely or properly included in data analysis. To this end, we have employed a combination of analytical theory, numerical simulations, and experiments with a commercial FSR and fluids of widely varying viscosity to elucidate the OSFR response over a large range of Ca. In undertaking this study, we had two key objectives in mind. First, to provide the minimal theoretical model necessary for interpreting surface-tension effects in OSFR measurements. Such a model ideally should make explicit the dependence of the measured force on experimentally controlled parameters and, if possible, be expressed in closed analytical form in favor of purely numerical results. Our secondary objective is to assess the ability of OSFR to infer surface tension in cases where it is unknown and quantify the uncertainty of such measurements. The latter is a key step if one hopes to extend the capabilities of OSFR to measure the surface properties of liquids as a function of time.

Our study is novel in several respects. First, we have validated theoretical predictions of OSFR over a range of capillary numbers not previously investigated, using both experiments and numerical simulations. In particular, our experimental work demonstrates the ability of OSFR to measure surface-tension forces with negligible contribution from viscous stresses, which has hitherto never been demonstrated. Our numerical work highlights the range of applicability of analytical theory and the breakdown of certain simplifying assumptions. Second, by critically analyzing the two limiting regimes of low- and high-viscosity fluids, we are able to develop an analytical prediction for the primary harmonic mode of the force response that spans these two regimes with quantitative accuracy. In this sense, our theoretical work uni-

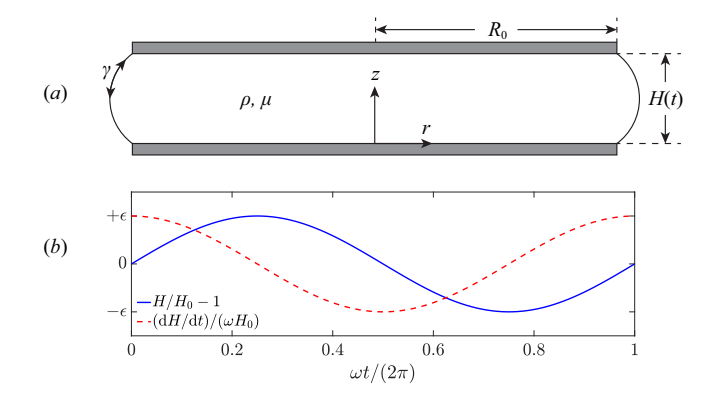


FIG. 1. (a) Schematic of the OSFR geometry and (b) the associated plate height and velocity. At time t=0, the film is a cylindrical column of initial height  $H_0$  and radius  $R_0$ , with aspect ratio  $\Lambda = H_0/(2R_0)$ . During squeeze flow, the height and radius are deformed to H(t) and R(z,t), respectively.

fies and extends previously developed models for OSFR, and illustrates key differences in the force response due to surface and bulk stresses. Finally, we have identified and implemented several key factors to ensure accurate force measurements of low fluid viscosities (low capillary numbers). These newfound insights will enable future development of instrumentation for measuring interfacial phenomena using liquid bridges. We envision such tools will be particularly useful for measuring interfacial properties of liquid metals, whose material-response functions are often dominated by the properties of stiff surface oxide layers. <sup>46</sup>

The remainder of the article is organized as follows. In §II, we present the governing theory for interpreting OSFR measurements, including the effect of surface tension. In §III, we compare our theoretical predictions to experiments using a commercial FSR in OSFR mode, and quantify the uncertainty in using the technique to measure surface tension. A discussion of our results is presented in §IV. Concluding remarks are given in §V.

#### II. THEORY

A schematic of the OSFR geometry is presented in Fig. 1. A Newtonian fluid (density  $\rho$ , viscosity  $\mu$ , surface tension  $\gamma$ ) is sandwiched between two plates of radius  $R_0$ , initially separated by a distance  $H_0$ . The bottom plate is held in a fixed position, while the top plate oscillates sinusoidally with an angular frequency  $\omega$  and amplitude  $\varepsilon H_0$  so that the instantaneous plate-plate separation at time t is

$$H(t) = H_0[1 + \varepsilon \sin(\omega t)]. \tag{1}$$

The force F(t) is measured at the bottom plate as a function of time. Neglecting the effects of inertia, gravity, and surface tension, one expects a perfectly viscous response from the squeeze flow of a Newtonian liquid. A lubrication analysis

of the squeeze flow yields the classical Stefan equation, 2,48-51

$$F(t) = \frac{3\pi\mu R_0^4}{2H^3} \frac{\mathrm{d}H}{\mathrm{d}t},\tag{2}$$

which relates the measured force F(t) to the controlled height H(t) through the viscosity  $\mu$ .

Several extensions of the Stefan equation (2) that have been discussed in the literature account for viscoelasticity, fluid inertia, and extensional flow. In the limit of small strains ( $\varepsilon \ll 1$ ), Pipkin's correspondence principle<sup>52</sup> can be used to transform Eq. (2) into a relation governing the response of a linearly viscoelastic material.<sup>49,50,53</sup> Inertial effects contribute an O(Re) correction to Eq. (2),<sup>2,54</sup> where  $\text{Re} = \rho \omega H_0^2/\mu$  is the Reynolds number, and are typically negligible for fluids of high viscosity (e.g., polymeric liquids). Spiegelberg, Ables, and McKinley <sup>51</sup> and later Wingstrand *et al.*<sup>2</sup> determined corrections to the Stefan equation due to extensional flow. The relative importance of extension compared to shear augments Eq. (2) by a factor  $(1+8\Lambda^2)$  [cf. Eq. (42) in Wingstrand *et al.*<sup>2</sup>], where  $\Lambda = H_0/(2R_0)$  is the aspect ratio of the undeformed liquid bridge. The latter results in the corrected Stefan equation,

$$F(t) = \frac{3\pi\mu R_0^4}{2H^3} \left( 1 + \frac{2H_0^2}{R_0^2} \right) \frac{dH}{dt},\tag{3}$$

which neglects the effects of viscoelasticity and inertia.

As was discussed in §I, additional *hydrostatic* corrections due to gravity and surface tension are typically omitted in the Stefan equation. Respectively, these effects become relevant at small values of the inverse gravity number  $Gr^{-1} = \mu \omega/(\rho g H_0)$  and capillary number  $Ca = \mu \omega R_0/\gamma$ . We have shown independently that gravitational effects do not significantly influence OSFR under most reasonable operating conditions (data available in the Supplemental Material, §S.3), with the main change being a static (time-independent) change to the force. Below, we show this is not the case for surface tension, which exhibits a non-trivial static and dynamic response.

# A. Thin-film, small-strain limit

It is instructive to first consider the effect of surface tension in the small-strain, small-aspect-ratio limit of OSFR ( $\varepsilon \ll 1$ ,  $\Lambda^2 \ll 1$ ), which corresponds to the weak oscillatory deformation of a thin, cylindrical liquid bridge. In what follows, axisymetrical cylindrical coordinates (r,z) are conveniently adopted, with r denoting the radial coordinate and z the axial coordinate (see Fig. 1). Inertial and gravitational effects will be neglected.

We begin by analyzing the kinematics of the flow. Phan-Thien <sup>49</sup> and others<sup>2,51</sup> derived the following incompressible velocity field for oscillatory squeeze flow [cf. Eqs. (18)-(19) in Phan-Thien <sup>49</sup>]:

$$u_r(r,z,t) = -\frac{3rz}{H_0^2} \left(1 - \frac{z}{H_0}\right) \frac{dH}{dt},$$
 (4a)

$$u_z(r,z,t) = \frac{z^2}{H_0^2} \left( 3 - \frac{2z}{H_0} \right) \frac{dH}{dt},$$
 (4b)

which is asymptotically valid for  $\varepsilon \ll 1$  and  $\Lambda^2 \ll 1$ . The above velocity field determines how the free surface r = R(z,t) evolves in time. Within the framework of small deformations from a cylindrical bridge of radius  $R_0$ , we have  $R \approx R_0$  and the kinematic condition at the free surface simplifies to

$$\begin{split} \frac{\partial R}{\partial t} &= u_r(R_0, z, t) \\ &= -\frac{3R_0 z}{H_0^2} \left( 1 - \frac{z}{H_0} \right) \frac{\mathrm{d}H}{\mathrm{d}t} \quad \text{by Eq. (4a)}. \end{split} \tag{5}$$

Here,  $u_r$  has been transferred to the *undeformed* surface  $r = R_0$ , incurring small errors of  $O(\varepsilon^2)$  and  $O(\Lambda^4)$ . Integrating Eq. (5) in time subject to the initial condition,

at 
$$t = 0$$
: 
$$R = R_0, \tag{6}$$

yields the parabolic shape profile.

$$R(z,t) = R_0 \left[ 1 - \frac{3z}{H_0} \left( 1 - \frac{z}{H_0} \right) \left( \frac{H}{H_0} - 1 \right) \right]. \tag{7}$$

This expression is linear in H(t) and thus predicts a sinusoidal shape response that is exactly in-phase with the plate-plate separation [cf. Eq. (1)].

Next, the liquid pressure p(r,t) generated by the viscous shearing forces must be determined. According to classical lubrication theory,<sup>55</sup> the pressure obeys the Reynolds lubrication equation,

$$\frac{1}{r}\frac{\partial}{\partial r}\left(r\frac{\partial p}{\partial r}\right) = \frac{12\mu}{H_0^2}u_z(r, H_0, t)$$

$$= \frac{12\mu}{H_0^2}\frac{dH}{dt} \quad \text{by Eq. (4b)}, \tag{8}$$

where we have approximated  $H \approx H_0$  on the right-hand side. Equation (8) may be integrated with respect to r, subject to the symmetry condition at the centerline,

at 
$$r = 0$$
:  $\frac{\partial p}{\partial r} = 0$ , (9a)

as well as a boundary condition at the surface  $r = R_0$  of the *undeformed* bridge. In typical analyses of OSFR, <sup>2,49</sup> one sets  $p(R_0,t)$  equal to the ambient pressure at the edge of the liquid, which neglects the capillary pressure jump due to surface tension. Here, we account for this jump in pressure by linearizing the curvature of the free surface for small deformations:

at 
$$r = R_0$$
: 
$$p = \gamma \left( \frac{1}{R_0} - \frac{\partial^2 R}{\partial z^2} \right). \tag{9b}$$

Thus, the effect of surface tension  $\gamma$  emerges in the pressure boundary condition (9b) at the free surface. Since the axial curvature  $\partial^2 R/\partial z^2$  is independent of z according to Eq. (7), then Eqs. (8)-(9) may be straightforwardly integrated to yield

$$p(r,t) = \gamma \left(\frac{1}{R_0} - \frac{\partial^2 R}{\partial z^2}\right) - \frac{3\mu}{H_0^3} \frac{\mathrm{d}H}{\mathrm{d}t} (R_0^2 - r^2)$$

$$= \gamma \left[ \frac{1}{R_0} - \frac{6R_0}{H_0^2} \left( \frac{H}{H_0} - 1 \right) \right] - \frac{3\mu}{H_0^3} \frac{dH}{dt} (R_0^2 - r^2). \tag{10}$$

The second term on the right-hand side of (10) is the cosinusoidal (out-of-phase) pressure response for oscillatory squeezing of a viscous liquid [see also Eq. (21) of Phan-Thien <sup>49</sup> and Eq. (29) of Spiegelberg, Ables, and McKinley <sup>51</sup>]. The first term is a correction due to the capillary pressure jump, which consists of a constant part that is proportional to the azimuthal curvature  $1/R_0$  as well as a sinusoidal (in-phase) part that is proportional to the axial curvature  $\partial^2 R/\partial z^2$ .

With the pressure determined by Eq. (10), the force F(t) on the bottom plate may now be calculated. This force consists of two contributions: a "bulk" contribution given by the integral of the axial stress over the bottom plate, and a "surface" contribution given by the surface-tension force at the edge of the plate. To leading order in  $\varepsilon$  and  $\Lambda^2$ , one finds

$$F(t) = -2\pi \int_0^{R_0} rp(r,t) dr + 2\pi \gamma R_0$$

$$= \pi \gamma R_0 \left[ 1 + \frac{6R_0^2}{H_0^2} \left( \frac{H}{H_0} - 1 \right) + \frac{3\mu R_0^3}{2\gamma H_0^3} \frac{dH}{dt} \right]. \tag{11}$$

Clearly, the last term in Eq. (11) is the classical Stefan result [cf. Eq. (2)] simplified to the small-strain limit,  $H \approx H_0$ . The additional terms are corrections due to surface tension. After inserting Eq. (1) for H(t) and introducing the dimensionless variables  $\tau = \omega t$  and  $\mathscr{F} = F/(\pi \gamma R_0)$ , one obtains the non-dimensionalized equation,

$$\mathscr{F}(\tau) = 1 + \frac{3}{2} (\varepsilon / \Lambda^2) \left( \sin \tau + \frac{1}{4} \text{Ca} \cos \tau \right), \tag{12}$$

where, as a reminder,  $\varepsilon$  is the axial strain amplitude,  $\Lambda = H_0/(2R_0)$  is the aspect ratio, and  $\text{Ca} = \mu \omega R_0/\gamma$  is the capillary number.

Equation (12) is the dimensionless linear-response function for OSFR measurements of a Newtonian fluid with constant surface tension. The viscous (loss) terms scales linearly with the capillary number Ca, as expected. The elastic (storage) term arises due to surface tension; in particular, it is the axial curvature  $\partial^2 R/\partial z^2$  that gives the sinusoidal response. The primary harmonic of the response function can be computed by taking the finite Fourier transform,

$$\mathscr{F}_1 \equiv \frac{1}{2\pi} \int_0^{2\pi} \mathscr{F}(\tau) e^{-i\tau} d\tau = \frac{3}{4} (\varepsilon/i\Lambda^2) \left(1 + \frac{1}{4}iCa\right), \quad (13)$$

for which the circuit analog is a spring (capacitor) and a dashpot (resistor) arranged in parallel (i.e., a Kelvin-Voigt model). A similar mechanical model was applied by Valsamis, Mastrangeli, and Lambert<sup>45</sup> to describe their experiments.

To benchmark the accuracy of the thin-film, small-strain model, we numerically simulated the full OSFR response using the finite element method (FEM) in COMSOL Multiphysics<sup>®</sup> (Version 5.5). In our FEM simulations, the coupled Navier-Stokes equations and free-surface deformation were posed and solved using the Laminar Two-Phase Flow and Moving Mesh interfaces. Briefly, the axisymmetric liquid film was represented by a rectangle in the *rz* plane

and discretized using triangular elements (the mesh spacing was refined as needed, depending on the strain amplitude and aspect ratio, to achieve convergent and accurate results). For a given parameter set, a time-dependent study was run using the backward differentiation formula (BDF) for time stepping. The absolute tolerance of the time-dependent solver was set to  $10^{-4}$  and applied to the (scaled) velocity field in the spatial configuration. At each time point, the force on the bottom plate was computed by applying a numerical quadrature and Fourier-transformed in time to obtain the first harmonic response.

Fig. 2 compares the predictions of Eq. (12) against our FEM simulations. In this figure, we have fixed the strain amplitude  $\varepsilon = 10\%$  and aspect ratio  $\Lambda = 1/8$ , which are typical parameters for the experiments presented in §III. Two values of the capillary number are shown [Ca = 120 (Fig. 2a) and Ca = 0.012 (Fig. 2b)] to isolate the viscous- and surfacetension-dominated contributions to the force. Although the qualitative features of the response – phase and approximate amplitude – are well captured by the the thin-film, small-strain model in the large- and small-Ca regimes, quantitative discrepancies exist due to nonlinear effects. These discrepancies vanish as the applied strain  $\varepsilon$  tends to zero, but, as will be discussed further in §III, this typically results in poor signal-tonoise ratios in experiments. Accounting for nonlinear effects - i.e., relaxing the constraints placed on  $\varepsilon$  and  $\Lambda$  - results in the green solid curves in Fig. 2, which quantitatively agree with the FEM-simulated response. These effects are discussed in detail in the next section.

# B. Finite- $\varepsilon$ and $\Lambda$ effects

In the previous section, a linear-response model for the dimensionless force  $\mathscr{F}(\tau)$  was derived by assuming small strains and small aspect ratios,  $\varepsilon \ll 1$  and  $\Lambda^2 \ll 1$ . This derivation resulted in Eq. (12) and its Fourier transform (13). On comparing this model to a high-fidelity simulation of OSFR using FEM, quantitative discrepancies were identified (Fig. 2). The objective of this section is to rectify those discrepancies by going beyond the thin-film, small-strain regime.

# 1. Viscous regime ( $Ca \gg 1$ )

We first revisit the well-studied<sup>1,2,49,53,56,57</sup> regime of large Ca, for which the force response is dominated by viscous effects. In the thin-film, small-strain limit, these effects are captured by the last term in Eq. (12) or, in terms of dimensional variables, Eq. (11). Two obvious improvements can be made to the large-Ca prediction of OSFR:

- Accounting for finite-ε effects. These amount to replacing H<sub>0</sub><sup>3</sup> with H<sup>3</sup> in the denominator of the last term in Eq. (11). The result is equivalent to the Stefan expression (2).
- Accounting for finite- $\Lambda$  effects. Wingstrand *et al.* <sup>2</sup> [Eq. (42)] showed that a weak extensional contribution to the

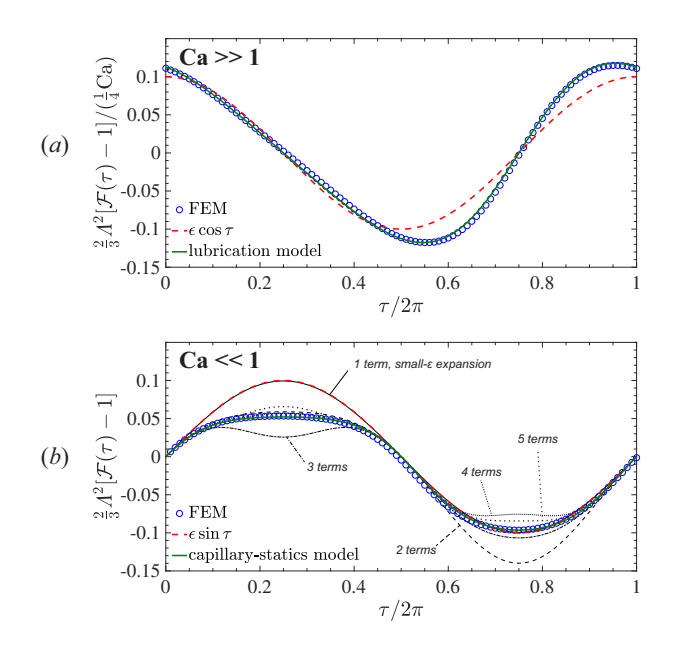


FIG. 2. Dimensionless force  $\mathscr{F}(\tau)$  plotted against dimensionless time  $\tau$  for one period of oscillation. (a) Viscous response for Ca = 120. (b) Elastic (surface-tension) response for Ca = 0.012. The other parameters are  $\varepsilon = 10\%$  and  $\Lambda = 1/8$ . Blue markers show the "exact" prediction by FEM; red dashed curves show the linear response predicted by Eq. (11); green solid curves show the full nonlinear response. In (b), light black curves show successive approximations of the nonlinear (capillary-statics) model by a small- $\varepsilon$  expansion [cf. Eq. (21)].

shear-dominated flow augments the Stefan result by a factor  $(1+8\Lambda^2)$ . The corrected expression is given by Eq. (3).

When these two effects are considered, one obtains the following expression – the so-called "lubrication model" – for the dimensionless force in the limit as  $Ca \rightarrow \infty$ :

$$\mathscr{F}(\tau) = \frac{3}{8} \operatorname{Ca}\left(\frac{1 + 8\Lambda^2}{\Lambda^2}\right) \frac{\varepsilon \cos \tau}{(1 + \varepsilon \sin \tau)^3}, \tag{14}$$

which is plotted in Fig. 2a (green curve). This expression clearly captures the nonlinear temporal response in the viscous regime,  $Ca \gg 1$ . Upon Fourier transformation (considering again only the primary harmonic), Eq. (14) becomes

$$\mathcal{F}_{1} = \frac{3}{16} \operatorname{Ca} \left( \frac{1 + 8\Lambda^{2}}{\Lambda^{2}} \right) \left( \frac{\varepsilon}{(1 - \varepsilon^{2})^{3/2}} \right)$$
$$= \frac{3}{16} \operatorname{Ca} (\varepsilon/\Lambda^{2}) \left( 1 + 8\Lambda^{2} \right) \left( 1 + \frac{3}{2} \varepsilon^{2} + \frac{15}{8} \varepsilon^{4} + \cdots \right), \quad (15)$$

where the last expression is a power series in  $\varepsilon^2$ . Obviously, higher harmonics ( $\mathscr{F}_2$ ,  $\mathscr{F}_3$ , etc.) are also included in the full nonlinear expression (14). However, these terms are appreciably weaker by successive powers of  $\varepsilon$  and, for our present purpose, not of immediate interest.

The amplitude  $|\mathcal{F}_1|$ , as given by Eq. (15), is plotted in Fig. 3 against the strain amplitude  $\varepsilon$  for three different aspect ratios  $\Lambda = 1/10$ , 1/8, and 1/6. Also shown are results

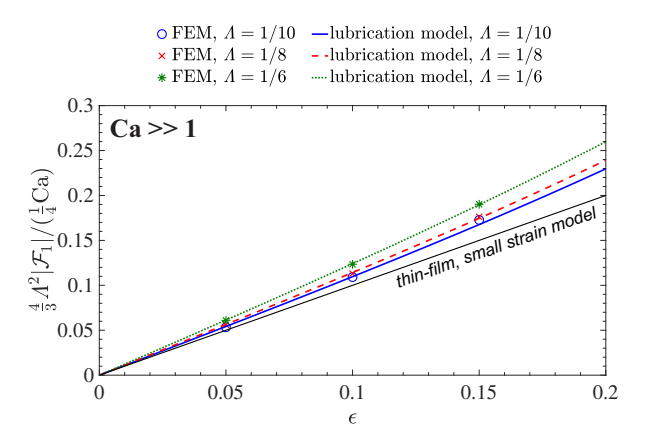


FIG. 3. Primary harmonic amplitude of the force plotted against the strain amplitude  $\varepsilon$  at three different aspect ratios  $\Lambda$  for a high-viscosity fluid (Ca = 120). The lubrication model is given by Eq. (15). Although the force is approximately linear up to strains of around 20%, the slope is modified from the thin-film, small-strain model due to finite- $\Lambda$  effects.

from FEM simulations, which show excellent agreement and demonstrate the validity of the lubrication model over a wide range of strain amplitudes and aspect ratios. Figure 3 clearly indicates a near-linear dependence of  $|\mathcal{F}_1|$  on  $\varepsilon$  for the range of strain amplitudes shown. The quantitative differences for different values of  $\Lambda$  are due to the prefactor  $(1+8\Lambda^2)$  introduced in Eq. (3). By comparison, finite- $\varepsilon$  corrections provide only a minor improvement.

The lubrication model presented above for OSFR at large Ca is well established in the existing literature. In the next section, we consider the opposite limit (Ca  $\rightarrow$  0) and the effect of surface tension on OSFR.

# 2. Capillary-statics regime (Ca $\ll 1$ )

For small Ca, viscous stresses are unimportant to the squeeze flow and the force response is dominated by surface tension. Figure 2b clearly shows that the linearized model (a pure sinusoid) does not capture the full temporal response of OSFR at small Ca. Geometric nonlinearities emerge because the squeezing motion of a thin film generates large changes in surface curvature. This can be deduced by examining the parabolic model for R(z,t) [Eq. (7)] and the axial curvature  $\partial^2 R/\partial z^2 = 6(R_0/H_0^3)(H-H_0)$ . For small  $\varepsilon$  and  $\Lambda$ , the axial curvature scales as  $\partial^2 R/\partial z^2 \sim \varepsilon/\Lambda^2 R_0$ , which is small compared to the azimuthal curvature  $1/R_0$  only if  $\varepsilon \ll \Lambda^2$ . This is a severe restriction to place on the strain amplitude to ensure "small" deformations. For even modest strains, the axial curvature can be on equal footing with (or larger than) the azimuthal curvature. Moreover, small changes in liquid height, which naturally occur during a period of oscillation, result in large changes in axial curvature that, in turn, can overwhelm the azimuthal curvature. In other words, the "near-cylinder" assumption is not uniformly valid for all times.

The key approximation that leads to the failure of the thinfilm, small-strain model at small Ca is the linearization (9b) of the stress boundary condition. The exact expression in the "static limit" (Ca  $\rightarrow$  0) is the Young-Laplace equation of cap-

$$p = \gamma \left( \frac{1}{R\sqrt{1 + (\partial R/\partial z)^2}} - \frac{\partial^2 R/\partial z^2}{[1 + (\partial R/\partial z)^2]^{3/2}} \right), \quad (16)$$

which is a nonlinear differential equation for R(z,t). To obtain the force on the bottom plate, Eq. (16) is first rearranged to form a total derivative:9

$$\frac{\partial F}{\partial z} \equiv \frac{\partial}{\partial z} \left( -\pi R^2 p + \frac{2\pi \gamma R}{\sqrt{1 + (\partial R/\partial z)^2}} \right) = 0. \tag{17}$$

The first integral of this expression, evaluated at z = 0, gives the desired force:

$$F(t) = -\pi R_0^2 p + \frac{2\pi \gamma R_0}{\sqrt{1 + (\partial R/\partial z)^2|_{z=0}}},$$
 (18)

which depends only upon time t as p(t) is spatially uniform in the static limit. Both p(t) and R(z,t) depend only parametrically on time through the position – but not the velocity - of the upper plate. This temporal dependence is expressed through the boundary conditions,

at 
$$z = 0$$
,  $H(t)$ :  $R = R_0$ , (19a)

which together with the fixed-volume constraint,

$$\int_0^{H(t)} \pi R^2 \, \mathrm{d}z = \pi R_0^2 H_0, \tag{19b}$$

completely specify the solution for R(z,t), p(t), and F(t). Gillette and Dyson <sup>19</sup> and others <sup>58,59</sup> derived a closed-form, though cumbersome, solution of Eqs. (16)-(19) in terms of elliptic integrals. A more direct solution procedure is to numerically integrate Eqs. (16)-(19) using the shooting method,

which is now the standard method for solving the axisymmetric Young-Laplace equation. We have applied this method for a range of strain amplitudes  $\varepsilon$  and aspect ratios  $\Lambda$  to calculate force F(t) over one period of oscillation (details of our shooting scheme can be found in the Supplemental Material, §S.1 A). To obtain the dimensionless force, we divide Eq. (18) through by  $\pi \gamma R_0$  and obtain

$$\mathscr{F}(\tau) = -\chi(\tau) + 2\cos\alpha_0(\tau),\tag{20}$$

where  $\chi = R_0 p / \gamma$  is the dimensionless pressure and  $\cos \alpha_0 =$  $1/\sqrt{1+(\partial R/\partial z)^2|_{z=0}}$  is the cosine of the liquid contact angle at the edge of the plate. To arrive at the linearized form [Eq. (11)], one need only make the near-cylinder approximation  $\cos \alpha_0 \approx 1$ .

Numerical evaluation of Eq. (20) gives the "exact" temporal response in the small-Ca limit, as shown in Fig. 2b via comparison to our FEM simulations of the squeeze flow at small, but finite, Ca. However, for the purpose of facile interpretation of OSFR measurements, it is desirable to have an analytical model of the surface-tension response in lieu of tabulated numerical results. Valsamis, Mastrangeli, and Lambert 45 derived analytical approximations of the surfacetension force by modeling an azimuthal section of the free surface as either a parabola or a circular arc (the circular arc providing the more accurate prediction). The resulting expressions, which depend upon the instantaneous edge angle  $\alpha_0(t)$ and height H(t), do not clearly reflect the dependence on the strain amplitude  $\varepsilon$  and aspect ratio  $\Lambda$ , which are the primary control parameters in an experiment. Below, we adopt an alternative approach that builds upon the thin-film, small-strain analysis of §II A.

Rather than posit an ansatz for the free-surface shape, we have developed a series of successive approximations to Eqs. (16)-(19) in powers of  $\varepsilon$  and  $\Lambda^2$ . The mathematical details of our perturbation analysis can be found in Appendix A. The main results of this analysis are double power-series expansions for the dimensionless force.

$$\mathcal{F}(\tau) = 1 + \frac{3}{2} (\varepsilon/\Lambda^2) (1 - \frac{2}{5}\Lambda^2 + \dots) \sin \tau - \frac{243}{40} (\varepsilon^2/\Lambda^2) (1 - \frac{2}{35}\Lambda^2 + \dots) \sin^2 \tau - \frac{81}{80} (\varepsilon^3/\Lambda^4) (1 - \frac{1556}{105}\Lambda^2 + \frac{94}{315}\Lambda^4 + \dots) \sin^3 \tau + \frac{34,749}{4480} (\varepsilon^4/\Lambda^4) (1 - \frac{2708}{715}\Lambda^2 + \frac{16,462}{495,495}\Lambda^4 + \dots) \sin^4 \tau + \frac{37,179}{44,800} (\varepsilon^5/\Lambda^6) (1 - \frac{1798}{45}\Lambda^2 + \frac{5,935,411}{98,175}\Lambda^4 - \frac{1,457,962}{5,221,125}\Lambda^6 + \dots) \sin^5 \tau + \dots,$$
(21)

and the first peak in its Fourier transform,

$$\mathscr{F}_{1} = \frac{3}{4} (\varepsilon / i\Lambda^{2}) [(1 - \frac{2}{5}\Lambda^{2} + \cdots) - \frac{81}{160} (\varepsilon^{2} / \Lambda^{2}) (1 - \frac{1556}{105}\Lambda^{2} + \frac{94}{315}\Lambda^{4} + \cdots) + \frac{12,393}{35,840} (\varepsilon^{4} / \Lambda^{4}) (1 - \frac{1798}{45}\Lambda^{2} + \frac{5,935,411}{98,175}\Lambda^{4} - \frac{1,457,962}{5,221,125}\Lambda^{6} + \cdots) + \cdots].$$
(22)

These expansions exhibit the correct limiting behavior as  $\varepsilon, \Lambda^2 \to 0$ . As compared to the lubrication model for  $\mathscr{F}_1$  [Eq.

(15)], the capillary-statics model (22) clearly exhibits a more complex and convoluted dependence on  $\varepsilon$  and  $\Lambda^2$ . Indeed,

the perturbation series (21)-(22) converge slowly if the ratio  $\varepsilon/\Lambda^2$  is not O(1), restricting direct application of the series to weakly nonlinear deformations. This can be clearly seen in Fig. 2b, where several truncations of Eq. (21) are plotted (as thin, black curves) and exhibit significant deviations from the exact solution during *either* the compression *or* the extension cycle of one full period. In particular, significant errors in extension, but not compression, occur when an odd number of terms is retained in the expansion (21). When instead an even number of terms is used, then the accuracy in extension is improved while the compression mode deviates from the exact solution.

The global accuracy of the Fourier-transformed series (22) can be considerably improved by recasting it in an alternative form.<sup>60</sup> For a reasonable range of  $\varepsilon$  and  $\Lambda$ , the following rational-fraction representation is particularly useful:

$$\mathscr{F}_{1} = \frac{3}{4} (\varepsilon / i\Lambda^{2}) \left[ \frac{1 - \frac{2}{5}\Lambda^{2} + \cdots}{1 + \frac{81}{160} (\varepsilon^{2} / \Lambda^{2}) (1 - \frac{1514}{105}\Lambda^{2} + \cdots)} \right], \tag{23}$$

where the higher-order terms have been omitted for simplicity. One can readily verify that Eq. (23) degenerates to (22) in the double limit as  $\varepsilon, \Lambda^2 \to 0$  while keeping the ratio  $\varepsilon/\Lambda^2$  finite. However, Eq. (23) has the additional benefit of remaining bounded as  $\Lambda^2 \to 0$  for any (finite)  $\varepsilon$ . This is an important advantage for thin films, for which  $\Lambda^2$  is typically small.

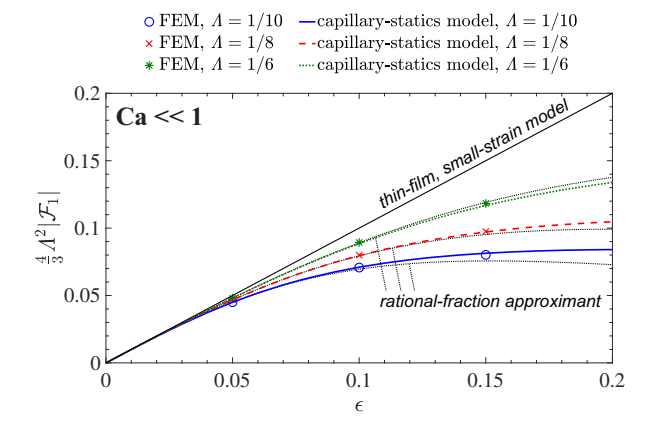


FIG. 4. Primary harmonic amplitude of the force plotted against the strain amplitude  $\varepsilon$  at three different aspect ratios  $\Lambda$  for a low-viscosity fluid (Ca = 0.012). The capillary-statics model is given by the numerical solution of Eqs. (16)-(19).

Figure 4 compares the rational-fraction approximant (23) to FEM simulations of the squeeze flow at small Ca as well as a direct numerical solution of Eqs. (16)-(20) via the shooting method. The analytical approximation, though highly simplified, exhibits reasonable agreement with the numerical results up to strains  $\varepsilon=20\%$  and, most significantly, gives the first "weakly nonlinear" correction at small, but finite,  $\varepsilon$ . In the double limit as  $\varepsilon, \Lambda^2 \to 0$ , the bracketed term in Eq. (23) simplifies to unity and we recover the first term in the thinfilm, small-strain model [Eq. (13)], also indicated in Fig. 4.

Clearly, the primary force amplitude is nonlinear in the strain amplitude, a marked departure from the viscous-dominated, lubrication model [cf. Fig. 3].

## C. Refined model

We now have two models for the linear OSFR response – i.e., the coefficient  $\mathscr{F}_1$  of the primary force harmonic – that properly take into account finite- $\varepsilon$  and  $\Lambda^2$  effects at either large or small Ca. As it is desirable to develop a model for any Ca, we take as a first approximation a simple superposition of Eqs. (15) and (23):

$$\mathscr{F}_1 \simeq \frac{3}{4} (\varepsilon / i\Lambda^2) \left( f_0 + \frac{1}{4} i Ca f_{\infty} \right),$$
 (24a)

where

$$f_{\infty} = \frac{1 + 8\Lambda^2}{(1 - \varepsilon^2)^{3/2}},\tag{24b}$$

$$f_0 \simeq \frac{1 - \frac{2}{5}\Lambda^2}{1 + \frac{81}{160}(\varepsilon^2/\Lambda^2)(1 - \frac{1514}{105}\Lambda^2)}$$
 (24c)

are prefactors that capture the appropriate finite- $\varepsilon$  and  $\Lambda^2$  effects in either limit of Ca. Clearly, the unified model [Eq. (24)] degenerates to the thin-film, small-strain model [Eq. (13)] in the double limit as  $\varepsilon, \Lambda^2 \to 0$ .

We wish to emphasize that the last expression [Eq. (24c)] is an approximation for small strains and moderately small aspect ratios. Table I compares Eq. (24c) to the "exact" numerical value of  $f_0$  for a reasonable range of strains and aspect ratios. The relative error in the approximation decreases considerably as  $\varepsilon$  or  $\Lambda$  is decreased while keeping the ratio  $\varepsilon/\Lambda^2 = O(1)$ . However, this approximation breaks down (large relative errors) when  $\varepsilon/\Lambda^2 \gg 1$ , as indicated by the third and sixth columns of Table I. The reason for this increase in error can be traced to the ascending sequence of terms in Eq. (22), which are omitted in Eq. (23), that scale with increasing powers of  $\varepsilon/\Lambda^2$ . When  $\varepsilon/\Lambda^2 \gg 1$ , these terms are non-negligible and an infinite number of terms must be summed to reproduce the exact result for the capillary force. Physically, this breakdown results from the large axial curvatures that can occur when a very thin film (small  $\Lambda^2$ ) is strained significantly enough  $(\varepsilon \gg \Lambda^2)$  such that it is no longer nearly cylindrical.

To assess the validity of Eq. (24), Fig. 5 plots the rescaled force amplitude,  $|\mathscr{F}_1^*| = \frac{4}{3}\Lambda^2|\mathscr{F}_1|/\varepsilon f_0$ , against a rescaled capillary number,  $\operatorname{Ca}^* = \frac{1}{4}\operatorname{Ca} f_{\infty}/f_0$ , including results from FEM simulations. The master curve predicted by Eq. (24a) collapses the numerical data reasonably well and correctly predicts the transition between the capillary-statics and viscous regimes at  $\operatorname{Ca}^* = 1$ . Only slight deviations from the exact results are observed in the capillary-statics regime ( $\operatorname{Ca}^* \to 0$ ) for extremely small aspect ratios and moderately small strains  $(\Lambda = 1/20, \varepsilon = 10\%)$ . This error is directly attributed to the approximation made in Eq. (24c); according to Table I, the relative error in  $f_0$  for  $\Lambda = 1/20$ ,  $\varepsilon = 10\%$  is about -17%. For larger aspect ratios in the range 1/8-1/5, which are more consistent with experimental measurements, this error decreases

	$f_0$				
$\boldsymbol{arepsilon}$	Λ	$\varepsilon/\Lambda^2$	exact	approx.	rel. error (%)
0.001	1/20	0.4	0.99881	0.99881	-0.0005
	1/8	0.064	0.99372	0.99373	0.0005
	1/5	0.2	0.98399	0.98399	0.0005
0.1	1/20	40	0.40946	0.33841	-17
	1/8	6.4	0.79637	0.79436	-0.25
	1/5	2.5	0.92616	0.93397	-0.84
0.2	1/20	80	0.18706	0.11342	-39
	1/8	12.8	0.52365	0.49588	-5.3
	1/5	5	0.76313	0.81037	6.2

TABLE I. Comparison of the "exact" numerical result for  $f_0$  to its rational-fraction approximant, Eq. (24c), for a selection of strains and aspect ratios.

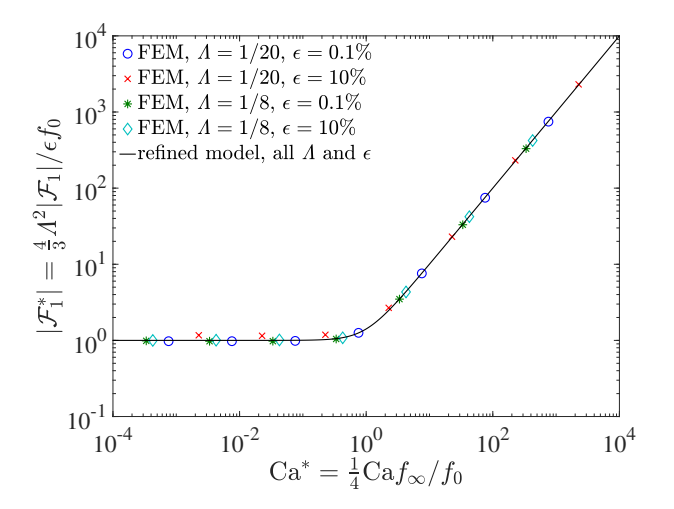


FIG. 5. Master curve plotting the rescaled force amplitude,  $|\mathscr{F}_1^*| = \frac{4}{3}\Lambda^2 |\mathscr{F}_1|/\varepsilon f_0$ , against a rescaled capillary number,  $\operatorname{Ca}^* = \frac{1}{4}\operatorname{Ca} f_{\infty}/f_0$ . The solid curve is given by Eq. (24a).

considerably. This gives us confidence in applying Eqs. (24) towards the interpretation of experimental measurements, presented in the following section.

### III. EXPERIMENTS

### A. Materials and methods

OSFR experiments were carried out on a commercial filament stretching rheometer (VADER 1000, *Rheo Filament*). Six test fluids (water, ethylene glycol, glycerol, polybutenes, silicone oil, and polyisoprene) were chosen to span a large range of Ca. The relevant physical properties of the fluids are presented in Table II. (Further details on the test fluids and shear measurements can be found in the Supplemental Material, §S.2 A). All fluids exhibited Newtonian behavior except polyisoprene, which shows shear-thinning behavior at high frequencies/rates. For polyisoprene, an average viscos-

Fluid	$\rho  (kg/m^3)$	μ (Pa s)	$\gamma (mN/m)$
Water	998	0.00094	72.0
Ethylene Glycol	1100	0.016	47.3
Glycerol	1261 <sup>†</sup>	0.86	53.0
Polybutenes	$890^{\dagger}$	31	22.4
Silicone Oil	971 <sup>†</sup>	100	35.0
Polyisoprene	920 <sup>†</sup>	$210\pm30$	$31.0^{\ddagger}$

TABLE II. Physical properties of the experimental test fluids († obtained from the supplier; ‡ obtained from van Krevelen and Te Nijenhuis <sup>61</sup>).

ity in the relevant frequency/rate range,  $0.1~\text{s}^{-1} < \dot{\gamma} < 20~\text{s}^{-1}$ , is reported in Table II (here,  $\dot{\gamma}$  is the shear rate). The error bars in the viscosity represent the standard deviation. Due to challenges in obtaining measurements of the surface tension of polyisoprene, data from van Krevelen and Te Nijenhuis <sup>61</sup> were used.

The VADER 1000 is equipped with matching stainless steel top and bottom plates with a diameter  $2R_0=6$  mm or 8 mm. Plates with smooth surfaces and sharp edges were used in order to promote full wetting and pinning of the fluid to the edge of the plates. The radius  $R_{\rm mid}(t)$  of the midplane of the liquid bridge is measured using a laser sheet, and the force F(t) is measured by a strain-gauge load cell on which the bottom plate is mounted. A sinusoidal displacement of the top plate is prescribed by the VADER controller:  $H_{\rm set}(t)=H_0\left[1+\varepsilon\sin(\omega t)\right]$ , where  $\varepsilon$  is the strain amplitude and  $\omega$  is frequency in rad/s, as shown in Fig. 1. The VADER 1000 outputs the prescribed height  $H_{\rm set}(t)$  and actual height H(t) as a function of time. The output was analyzed to confirm agreement between the prescribed and actual height displacements. In all cases, sinusoidal motions were observed.

# B. Experimental protocol

Prior to each experiment, the plates are carefully adjusted (by eye) to ensure they are parallel. The height measurement is zeroed by first lowering the top plate until it contacts the bottom plate and an appreciable force is measured. At the beginning of an experiment, the test fluid is loaded onto the bottom plate using a syringe. The top plate is then lowered slowly to contact the fluid such that the plates are fully wetted and the contact lines at the upper and lower plate edges are pinned. Before testing, the height of the liquid bridge is manually adjusted until the shape is cylindrical, as confirmed by laser micrometer scans of diameter across the entire height. Efforts were made to achieve consistent initial heights  $H_0 = 1 \pm 0.3$  mm. The force transducer is then tared to the weight of the sample and the surface-tension force of the cylindrical film. For highly viscous samples, the liquid bridge was allowed to reach an equilibrium shape (steady-state force) before taring.

Experiments were conducted over ten full oscillations. Averages of the measured height H(t), midplane radius  $R_{\rm mid}(t)$ , and force F(t) were taken over all ten periods along with their

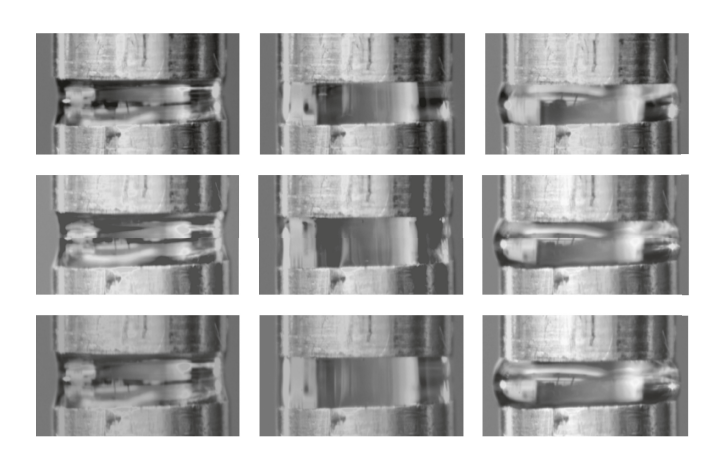


FIG. 6. Experimental images of glycerol undergoing oscillatory squeezing at several time points and oscillation frequencies. From top to bottom:  $\omega/(2\pi)=1$  Hz, 0.1 Hz, and 0.05 Hz. From left to right:  $\omega t=\pi/2$ ,  $\pi$ , and  $3\pi/2$ . For all experiments,  $\varepsilon=10\%$  and  $R_0=4$  mm.

associated standard deviations. The practical range of oscillation frequencies,  $\omega/(2\pi)$ , is between 0.01 Hz and 1 Hz, although lower frequencies are achievable if evaporation is negligible over the duration of the experiment. The experimental range of suitable strain amplitudes is bounded by the stability of the liquid bridge, which ensures that the contact line remains pinned and the film does not rupture<sup>24,25</sup>. The critical strain above which the contact line depins is about 12% for experimentally relevant aspect ratios in the range  $\Lambda=0.1$ -0.2 (further details can be found in the Supplemental Material, §S.4). The oscillation amplitude  $\varepsilon$  was maintained between 5% and 10%, which maximizes the signal-to-noise ratio while preserving the stability of the film.

Figure 6 shows micrographs of glycerol in a typical experiment at several time points and different oscillation frequencies. Videos were recorded during several experiments in order to verify that the film remains pinned to the plate edge. Successful pinning is clearly achieved and maintained throughout the experiment. However, slight plate misalignment is also evident, which has a significant impact on the measured surface-tension force. Slight depinning was observed in some cases for the silicone oil, especially at low frequencies, due to initial aspect ratios approaching the depinning instability. For this reason, all experiments reported for the silicone oil were conducted at frequencies  $\omega/(2\pi)$  > 0.1 Hz. We expect film depinning to have a small (quantitative) effect on the force measurement at high capillary numbers (Ca  $\gg$  1), since the surface-tension force is small compared to the viscous force in this regime.

# C. Experimental results and comparison to theory

Figure 7 shows two representative data sets for polyisoprene (Fig. 7a, corresponding to the high-Ca regime) and glycerol (7b, low-Ca regime). The height H(t), midplane radius  $R_{\rm mid}(t)$ , and force F(t) are averaged over ten cycles and

plotted for a single time interval. Also plotted in Figs. 7a and 7b are predictions based, respectively, on the lubrication model (presented in §II B 1) and the capillary-statics model (§II B 2). The model predictions are based on the measured height H(t) for each experiment. No fitting parameters were used in the theoretical predictions. Based on Fig. 7, the models clearly capture the important qualitative and quantitative features of the measured radius  $R_{\rm mid}(t)$  and force F(t). The slight overprediction of the radius and force by the two models is due to errors in the measured height, which were described in §III A and are discussed later in this section. We note that several "jumps" in the force F(t) are measured in Fig. 7a; these correspond to instantaneous jumps in the plate velocity, which result in a sudden increase or decrease in H(t).

The discrete Fourier transform of  $\mathscr{F}(\tau) = F(\omega t)/\pi \gamma R_0$  gives the primary harmonic amplitude  $|\mathscr{F}_1|$ . Figure 8 plots our measurements of  $|\mathscr{F}_1|$  against Ca for all experimental test fluids. The plot is normalized using the same convention as in Fig. 5 so that we may compare the experimental data against the predictions of Eq. (24a). For the normalization, the parameters  $\varepsilon$ ,  $\Lambda$ ,  $H_0$ , and  $R_0$  are computed from measurements of H(t) and  $R_{\text{mid}}(t)$ , as described in the Supplemental Material, §S.2 B. The meaning of the differently colored data points in Fig. 8 is described below.

The blue data points in Fig. 8 show qualitative agreement with the theoretical predictions, with increasing discrepancy at lower capillary numbers. These points were processed using the height measurement from the VADER 1000; a height offset of  $\Delta H = 83~\mu m$  was assumed due to error in the zeroing routine. However, uncertainty still exists in the measured height due to plate misalignment, which is difficult to determine without a secondary height measurement. The error bars in the blue data points are one-sided to reflect an additional uncertainty in the height corresponding to an estimated (maximum) misalignment  $\psi = 2^{\circ}$ , which translates to a height offset  $\Delta H_{\psi} = R_0 \sin \psi = 140~\mu m$  for a plate diameter of  $2R_0 = 8$  mm. The upper limit of the error window thus reflects a total offset of 223  $\mu m$  above the value reported by the instrument.

Several experiments were conducted using video imaging to accurately measure the average height as a function of time (details of this measurement can be found in the Supplemental Material, §S.2D). The red points in Fig. 8 correspond to experiments using the measured height from video microscopy. These experiments show much better agreement with theory, confirming the need for very accurate height measurement in the capillary-statics regime. However, significant discrepancies persist at much lower capillary numbers even after considering significant misalignment of the plates. There are two possible explanations for these discrepancies: (i) non-axisymmetric effects<sup>38</sup>, which are not accounted for in the theory discussed in §II, or (ii) low accuracy of the load cell. To investigate non-axisymmetric effects, we numerically solve the full Young-Laplace equation over the radius r and azimuthal angle  $\theta$ , subject to slight misalignment of the top and bottom plates (details may be found in the Supplemental Material, §S.1 B). Both misalignment of the plate centers [or eccentricity, as detailed in<sup>38,62</sup>] and misalignment perpendicular to the axis of symmetry are considered. In short, we

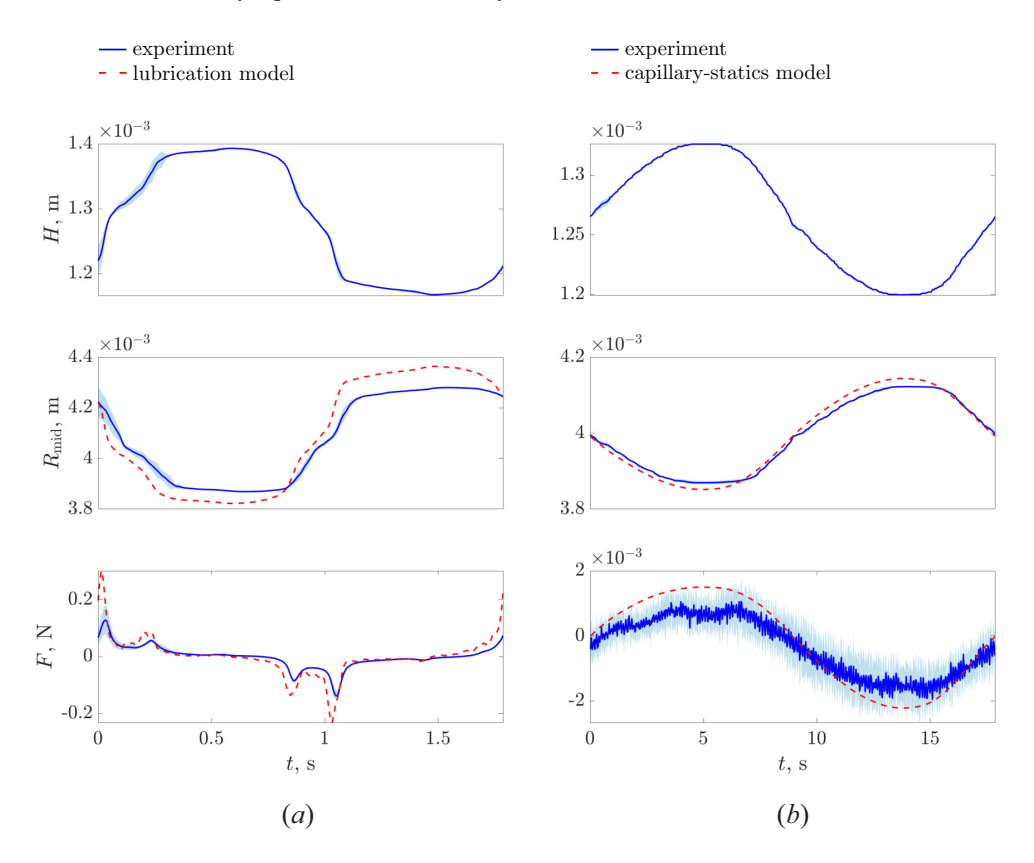


FIG. 7. Time series of the experimental height H(t), midplane radius  $R_{\rm mid}(t)$ , and force F(t) for (a) polyisoprene at  $\varepsilon=10\%$  and  $\omega/(2\pi)=0.56$  Hz (Ca = 97) and (b) glycerol at  $\varepsilon=5\%$  and  $\omega/(2\pi)=0.056$  Hz (Ca = 0.023). Solid curves and shaded regions indicate the mean and standard deviation, respectively, based on measurements taken over ten oscillation periods. Dashed curves indicate predictions from the lubrication and capillary-statics models based on the measured height.

find no significant change in the force when the average height is kept constant. Therefore, non-axisymmetric effects cannot accurately explain the discrepancy between experiment and theory, which leaves the accuracy of the load cell as the only reasonable explanation.

The blue and red points in Fig. 8 were measured using a load cell rated for 5 N with a nonlinearity error of  $2.5 \times 10^{-3}$ N. At low Ca, the force reading was as small as  $1 \times 10^{-3}$  N (see Fig. 7b), which is below the recommended threshold of the load cell and could lead to inaccuracies in the measured force amplitude. The green points in Fig. 8 show experiments with water and ethylene glycol (corresponding to the lowest capillary numbers) using a more sensitive load cell, which is rated for 1 N with a nonlinearity error of  $5 \times 10^{-4}$  N. As with the red data, the green data was processed using the height offset measured from video microscopy. However, the use of a more sensitive force transducer results in much better agreement with theory. Thus, when the height offset, misalignment, and load cell accuracy are all accounted for, quantitative agreement between theory and experiment is achieved over six decades in the capillary number.

The implications of these findings on OSFR are as follows. Firstly, the accurate measure of height is critical, as the force response in either the capillary-statics or viscous regimes largely depends on the initial height  $H_0$  and strain am-

plitude  $\varepsilon$ . Using the VADER 1000, these issues are magnified because of the increased aspect ratio, which leads to larger difficulty in manually aligning the plates. Note that the factor of two discrepancy in the force reported by Wingstrand *et al.* <sup>2</sup> (for viscoelastic moduli measured in the high-Ca limit) is most likely due to the height offset discussed above. Finally, the accuracy of the force transducer is an important instrument consideration because the forces measured in the capillary-statics regime are particularly small. However, this also suggests that the larger forces generated in the viscous regime may exceed the transducer limit, meaning different transducers would be required for the viscous and capillary-statics regimes.

# D. Evaluation of OSFR for measuring surface tension

Having verified the crossover from viscous- to surface-tension-dominated behavior at a critical capillary number  $Ca^*=1$ , we now assess the ability of OSFR to measure surface tension in the regime  $Ca^*\ll 1$  based on the amplitude of the oscillating force response. For this purpose, we focus only on the green data in Fig. 8 – those which were measured using the most sensitive force transducer with concurrent imaging of the shape profile. The test fluids considered – water and ethylene glycol – have the highest surface tension of any of the

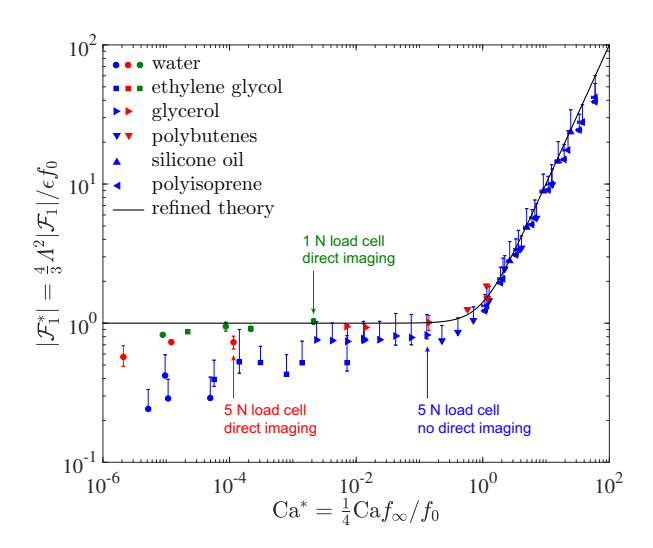


FIG. 8. Experimental measurements of the rescaled force amplitude,  $|\mathscr{F}_1^*| = \frac{4}{3}\Lambda^2|\mathscr{F}_1|/\varepsilon f_0$ , plotted against a rescaled capillary number,  $\operatorname{Ca}^* = \frac{1}{4}\operatorname{Ca} f_{\infty}/f_0$ . Blue points represent data using the measured height  $H(t) + \Delta H$ , assuming an offset of  $\Delta H = 83~\mu\mathrm{m}$  from the zeroing routine of the machine. Red and green points were processed using the average height offset measured from image-analyzed micrographs. Green points were also measured using a more sensitive force transducer. Error bars represent the standard deviation based on replicate errors, material property uncertainty, and plate misalignment.

test fluids studied (cf. Table II).

To use OSFR to measure surface tension, we assume that the density  $\rho$  and viscosity  $\mu$  are independently measured but leave the surface tension  $\gamma$  as an unknown parameter. OSFR measures the plate height  $H^{\rm exp}(\omega t)$  and force  $F^{\rm exp}(\omega t)$  simultaneously for a given frequency  $\omega$ . We may render the height and force dimensionless as  $\mathscr{H}(\tau) = H(\omega t)/H_0 - 1$  and  $\mathscr{F}(\tau) = F(\omega t)/\pi \gamma R_0$ . Given the experimentally measured height program,  $\mathscr{H}^{\rm exp}(\tau)$ , the dimensionless capillary force can be predicted theoretically,  $\mathscr{F}^{\rm thr}(\tau)$ , using Eq. (20). Thus, we may measure the surface tension by fitting our experimental measurements of the (dimensional) force  $F^{\rm exp}(\omega t)$  to the following model:

$$F^{\exp}(\omega t) = \pi \gamma R_0 \left\{ \mathscr{F}_0 + \mathscr{F}^{\text{thr}} \left[ \mathscr{H}^{\exp}(\tau) \right] \right\}, \qquad (25)$$

where  $\mathscr{F}_0$  is an offset (accounting for possible errors in the initial taring of the load cell) and  $\mathscr{F}^{thr}[\mathscr{H}^{exp}(\tau)]$  denotes the functional dependence of  $\mathscr{F}^{thr}$  on  $\mathscr{H}^{exp}$ .

In Eq. (25), the only unknown parameters are the surface tension  $\gamma$  and the force offset  $\mathcal{F}_0$ ; all other parameters are measured or known independently. We fit  $\gamma$  and  $\mathcal{F}_0$  using nonlinear least-squares regression with 95% confidence intervals (assuming normally distributed error). The resulting regression parameters at three different frequencies are tabulated in Tables III and IV for water and ethylene glycol, respectively; the associated force-time curves are presented in the Supplemental Material, §S.5. The fits for water give reasonable, albeit underestimated, measurements of surface tension in the range 58-68 mN/m (the exact value is 72 mN/m).

$\omega/2\pi$ (Hz)	0.01	0.1	1	1 (w/time shift)
γ (mN/m)	$64.7 \pm 0.4$	$58.8 \pm 0.3$	$51.5 \pm 3.5$	$67.4 \pm 1.2$
$\mathscr{F}_0$	2.01	1.00	0.675	0.537

TABLE III. Fit values of  $\gamma$  and  $\mathscr{F}_0$  for water at a strain  $\varepsilon=10\%$ , corresponding to the green data in Fig. 8. The exact surface tension of water is 72.0 mN/m. For the experiment at 1 Hz, a time shift  $\tau_{\rm shift}=-0.631$  dramatically improved the fit.

$\omega/2\pi$ (Hz)	0.01	0.1	1
γ (mN/m)	$40.5 \pm 0.1$	$41.1 \pm 0.4$	$53.1 \pm 1.3$
$\mathscr{F}_0$	0.0162	0.427	0.0005

TABLE IV. Fit values of  $\gamma$  and  $\mathscr{F}_0$  for ethylene glycol at a strain  $\varepsilon = 10\%$ , corresponding to the green data in Fig. 8. The exact surface tension of ethylene glycol is 47.3 mN/m.

The fits for ethylene glycol are generally more accurate, in the range 40-53 mN/m (the exact value is 47.3 mN/m). These data suggest that OSFR is capable of measuring the surface tension of low viscosity fluids to within 20% relative error with current instrumentation and protocol.

# IV. DISCUSSION

We have presented a comprehensive study of Newtonian fluids undergoing oscillatory squeeze flow in order to quantitatively predict the effect of surface tension on the measured force F(t). Equation (24), reproduced below for convenience,

$$\mathcal{F}_{1} \equiv \frac{F_{1}}{\pi \gamma R_{0}} = \frac{3\varepsilon}{4i\Lambda^{2}} \left( f_{0} + \frac{iCaf_{\infty}}{4} \right)$$

$$\simeq \frac{3\varepsilon}{4i\Lambda^{2}} \left[ \frac{1 - \frac{2}{5}\Lambda^{2}}{1 + \frac{81}{160}(\varepsilon^{2}/\Lambda^{2})(1 - \frac{1514}{105}\Lambda^{2})} + \frac{1}{4}iCa\left(\frac{1 + 8\Lambda^{2}}{(1 - \varepsilon^{2})^{3/2}}\right) \right], \quad (24)$$

accurately captures the influence of fluid flow and surface tension (Ca =  $\mu \omega R_0/\gamma$ ), strain amplitude ( $\varepsilon$ ), and initial aspect ratio [ $\Lambda = H_0/(2R_0)$ ], as verified by direct comparison to numerical simulations (Fig. 5) and experiments (Fig. 8) over several decades in a modified capillary number,

$$Ca^* = \frac{Ca f_{\infty}}{4f_0}$$

$$\simeq \frac{Ca}{4} \left( \frac{1 + 8\Lambda^2}{(1 - \varepsilon^2)^{3/2}} \right) \left( \frac{1 + \frac{81}{160} (\varepsilon^2 / \Lambda^2) (1 - \frac{1514}{105} \Lambda^2)}{1 - \frac{2}{5} \Lambda^2} \right). \tag{26}$$

This model for the primary harmonic force response is advantageous in that it clearly expresses the dependence on the capillary number Ca, strain amplitude  $\varepsilon$ , and aspect ration  $\Lambda$  in closed analytical form. The primary disadvantage of this

model is in the approximation for  $f_0$  [cf. Eq. (24c)], which breaks down when the ratio  $\varepsilon/\Lambda^2$  is not O(1).

For thin films  $\Lambda^2 \ll 1$  and sufficiently small strains  $\varepsilon =$  $O(\Lambda^2)$ , Eq. (24) simplifies to the thin-film, small-strain model (13). The small-strain model reflects the essential physics of the expected force response. The real part of this expression [in-phase with the plate velocity  $dH/dt = \varepsilon \omega H_0 \cos(\omega t)$ ] is essentially the classical lubrication prediction for OSFR based on the linearized Stefan equation (2). The imaginary part (outof-phase with the plate velocity) is a new contribution to the theory of OSFR, and represents the force of surface tension along the axial curvature  $1/R_2 \approx -(6\varepsilon R_0/H_0^2)\sin(\omega t)$  of the free surface. We find that this force is highly sensitive to the geometry of the film due to the  $H_0^{-2}$  dependence of the axial curvature. Therefore, this force can be amplified by simply reducing the initial thickness of the film; however, this reduction will constrain the experimentally accessible range of strain amplitudes. The azimuthal curvature,  $1/R_1 \approx 1/R_0$ , is approximately independent of t and, therefore, does not contribute to  $F_1$ .

Although the thin-film, small-strain model [Eq. (13)] exhibits a simpler dependence on  $\varepsilon$  and  $\Lambda$  as compared to the refined model [Eq. (24)], its applicability is limited to  $\Lambda^2 \ll 1$  and  $\varepsilon \sim \Lambda^2$ . The restriction of (13) to small strains ( $\varepsilon \ll 1$ ) applies mainly to the small-Ca (capillary-statics) regime, where the force is generally a nonlinear function of the applied strain  $\varepsilon$  (Fig. 4). This nonlinearity is well captured by the rational-fraction approximant, Eq. (23), of the capillary-statics response. At larger Ca (viscous regime), the force is approximately linear in the applied strain  $\varepsilon$  even for strains as large as 20% (Fig. 3). Thus, the factor of  $(1-\varepsilon^2)^{-3/2}$  appearing in Eq. (24) contributes only a small correction to the force response.

The additional restriction of Eq. (13) to thin films ( $\Lambda^2 \ll 1$ ) affects both the large-Ca and small-Ca regimes. In particular, at high Ca we expect an increase in the predicted force according to the factor of  $(1+8\Lambda^2)$  in Eq. (24), which was previously introduced by Wingstrand *et al.* <sup>2</sup> [cf. Eq. (3)]. This  $O(\Lambda^2)$  correction arises due to the relative importance of uniaxial extension as compared to shear in OSFR. According to Fig. 3, this correction is generally non-negligible under typical operating conditions. At low Ca, the dependence of the force on  $\Lambda$  is more complicated (Fig. 4), and is again captured by Eq. (23). Thus, finite- $\Lambda$  effects generally introduce quantitative corrections to the measured force for strain amplitudes  $\varepsilon$  greater than a few percent, regardless of the value of Ca.

The theoretical limitations of Eq. (13) are further compounded by practical considerations that arise in experiments. For one, the strain amplitude must be sufficiently large to achieve a good force signal-to-noise ratio. Smaller strains give a noisier force response F(t), adding unwanted uncertainty to the value of  $F_1$  upon Fourier transformation. On the other hand, large strains (>10%) can result in film squeezeout and contact line depinning due to a meniscus instability (see the Supplemental Material, §S.4). Thus, for all practical purposes, the strain set point is limited to the range  $\varepsilon \leq 10\%$  in our study. The aspect ratio is determined from simultaneous measurements of the film height and diameter, with typ-

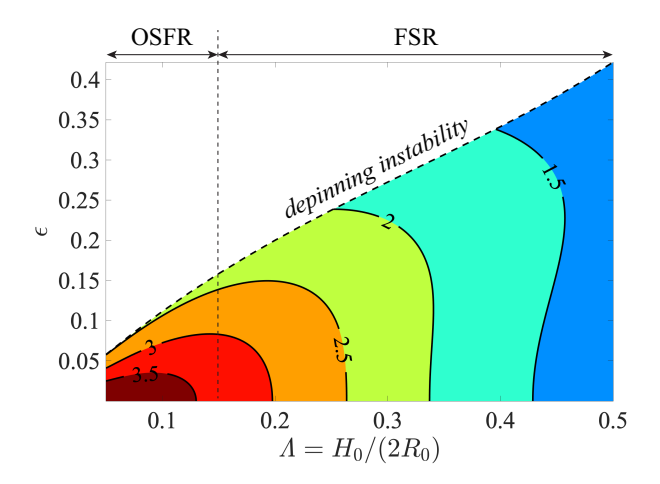


FIG. 9. Operating diagram for OSFR based on the isocontours  $Ca = Ca_c$ , as a function of  $\varepsilon$  and  $\Lambda$ , for which  $Ca^* = 1$ . The dashed line represents the magnitude of the minimum stable  $\varepsilon$ , corresponding to fluid ejection from the plates. The top labels indicate operating windows for conventional OSFR and the FSR in OSFR mode, based on typical aspect ratios.

ical values in the range  $\Lambda=0.1$ -0.2. For such small aspect ratios, Eq. (13) only holds for small strains, i.e., a few percent. Therefore, the more general model (24) is necessary to accurately predict the force response.

An operating diagram for OSFR and FSR can be constructed based on the criterion  $Ca^* = 1$ . Figure 9 plots the isocontours  $Ca = Ca_c$  as a function of  $\Lambda$  and  $\varepsilon$  that satisfy this criterion. Because Eq. (26) is an approximation that breaks down as  $\varepsilon$  or  $\Lambda$  is increased, the exact solution for  $f_0$  – rather than the rational fraction approximant, Eq. (24c) – was used to compute  $Ca^* = 1$  and the isocontours in Fig. 9 (see Figure S.1 in the Supplemental Material for plots of the exact values of  $f_0$  as a function of  $\varepsilon$  and  $\Lambda$ ). For fixed values of  $\varepsilon$  and  $\Lambda$ , the calculated Ca<sub>c</sub> represents the transition between the viscous and capillary-statics regimes; i.e., Ca > Ca<sub>c</sub> would result in forces dominated by viscosity, whereas Ca < Ca<sub>c</sub> gives a surface-tension-dominated response. In the limit as  $\varepsilon \to 0$ ,  $Ca_c \simeq (1 + 8\Lambda^2)/(1 - \frac{2}{5}\Lambda^2)$  and the transition is approximately independent of the (small) applied strain. The upper bound of  $\varepsilon$  is determined by the film stability limit, which corresponds to a limit on compression where the fluid is expelled from the plates (see the Supplemental Material, §S.4, for more details on film stability). Evidently,  $\Lambda$  is a much more important parameter than  $\varepsilon$  in defining  $Ca_c$ . Also indicated, at the top of the plot, are the typical operating windows for commercial OSFR instruments and the VADER 1000 in OSFR mode. Values of Ca > 4 for OSFR instruments, and greater than 2.5 for the VADER 1000, are sufficient to ignore surface-tension effects. This operating diagram places the experimental limitations on fluid viscosity that are measurable using oscillatory squeeze flow. For example, considering a frequency of  $\omega/(2\pi) = 10$  Hz, a surface tension of  $\gamma = 35$  mN/m, and a plate diameter of  $2R_0 = 25$  mm, the fluid viscosity should be greater than 0.09 Pa s to minimize surface-tension effects.

On the other hand, the low-Ca response suggests that the

OSFR method could be used to measure surface tension  $\gamma$  or, more generally, the dynamical surface properties of materials. We evaluated the capability of OSFR to measure surface tension in §III D, and found that, with current instrumentation and protocol, the surface tensions of water and ethylene glycol were measured to within an accuracy of 20% (relative error). It should be emphasized that our primary purpose for this evaluation was not to invent a new way to measure surface tension per se - indeed, numerous, more accurate measurement techniques for this purpose that date back a hundred years (e.g., Wilhelmy plate or pendant drop tensiometry). Rather, the advantage of OSFR as a measurement tool is to extract dynamic changes to surface tension through time-periodic changes in curvature. For instance, the OSFR technique could be applied to (i) measure the static surface tension  $\gamma$  of moderately viscous fluids; (ii) measure the dynamic surface tension  $\gamma(t)$  as a function of frequency to determine the adsorption or desorption of surface-active species to and from the interface; (iii) measure the surface viscoelastic properties of materials with negligible bulk stresses, e.g., the oxide films on the surface of liquid metals<sup>46</sup>. To these ends, our present evaluation is encouraging that OSFR, with suitable improvements, can be made into a valuable interfacial measurement tool akin to the oscillating bubble tensiometer. 63,64

Several aspects must be considered to optimize OSFR as an interfacial measurement technique. First, ensuring that the contact line remains pinned to the edge of the plates is critical. Second, the height measurements must be accurate. One method of ensuring accurate height measurements is the use of video microscopy and image analysis. Lastly, the amplitude of the force measured should be within the accuracy of the force transducer.

#### V. SUMMARY AND CONCLUSIONS

The key results of this work may be summarized as follows:

- We demonstrate that theoretical predictions of the OSFR primary harmonic force mode  $\mathscr{F}_1$  collapse onto a universal curve when plotted against a modified capillary number  $Ca^*$ . These predictions are robust for experimentally relevant values of the aspect ratio  $\Lambda$  and strain amplitude  $\varepsilon$ .
- For Ca\* >> 1, the force is driven primarily by viscous shear stresses and predicted by lubrication theory. This response can be modeled analytically with high fidelity.
- For Ca\*  $\ll$  1, the force is predicted by capillary statics. Modeling the capillary-statics response in general requires a numerical method, but a double perturbation expansion (recast as a rational fraction) provides a suitable approximation provided that  $\varepsilon$  and  $\Lambda^2$  are small and the ratio  $\varepsilon/\Lambda^2 = O(1)$ .
- Experimental measurements completed over a wide range of Ca\* compare favorably to theory and demonstrate, for the first time, the ability of OSFR to mea-

sure surface-tension forces in the absence of viscous stresses.

• Current measurements of surface tension using OSFR are accurate to within a relative error of 20%, with clear avenues for improvement.

The application of the present theory requires that the fluid is Newtonian and the interface has a constant surface tension and no surface viscosity (shear or dilatational). Future work will examine the effects of surface viscosity and non-Newtonian fluids.

# **NOMENCLATURE**

 $\alpha_0$  – liquid contact angle at the bottom plate

Ca – capillary number

Ca\* – modified capillary number

 $\chi$  – dimensionless pressure

 $\varepsilon$  – strain amplitude

 $f_0$  – low-Ca force factor

 $f_{\infty}$  – high-Ca force factor

F – force on the bottom plate

 $\mathcal{F}$  – dimensionless force

 $\mathcal{F}_1$  – primary harmonic mode of the dimensionless force

 $\mathscr{F}^*$  – modified dimensionless force

Gr - gravity number

 $\gamma$  – surface tension

H – liquid bridge height

 $H_0$  – initial liquid bridge height

 $i-imaginary \ unit \\$ 

 $\Lambda$  – aspect ratio

 $\mu$  – viscosity

p – pressure

r – radial position

R – liquid bridge radius

 $R_0$  – initial liquid bridge radius

Re - Reynolds number

 $\rho$  – density

t – time

 $\tau$  – dimensionless time

 $\theta$  – azimuthal angle

 $u_r$  – radial velocity component

 $u_z$  – axial velocity component

 $\psi$  – plate misalignment angle

 $\omega$  – angular frequency

z – axial position

## SUPPLEMENTAL MATERIAL

Online supplemental material contains (1) numerical methods for integration of the capillary-statics equations; (2) additional experimental details; (3) discussion of gravitational and inertial effects; (4) discussion of capillary bridge instabilities; and (5) raw OSFR data for fitting surface tension by nonlinear regression.

#### **ACKNOWLEDGMENTS**

The work of Z.R.H and N.J.A. was supported by the National Science Foundation under grant no. CBET-1847140.

## **CONFLICTS OF INTEREST**

The authors have no conflicts to disclose.

# **DATA AVAILABILITY**

The data that supports the findings of this study are available within the article and its supplementary material.

# Appendix A: Small-strain analysis of the capillary-statics model

In this Appendix, we derive an approximate solution to the capillary statics equations, Eqs. (16)-(19), for small strain amplitudes,  $\varepsilon \ll 1$ . In this regime, we may expand R, p, and F in perturbation series with respect to  $\varepsilon$ :

$$R(z,t) = R_0 + \varepsilon R^{(1)}(z,t) + \varepsilon^2 R^{(2)}(z,t) + \cdots,$$
 (A1a)

$$p(t) = \frac{\gamma}{R_0} + \varepsilon p^{(1)}(t) + \varepsilon^2 p^{(2)}(t) + \cdots, \qquad (A1b)$$

$$F(t) = \pi \gamma R_0 + \varepsilon F^{(1)}(t) + \varepsilon^2 F^{(2)}(t) + \cdots . \tag{A1c}$$

The leading-order terms in equation (A1) correspond to the unperturbed state (i.e., a cylindrical column of radius  $R_0$ ). We also make use of the boundary perturbations at z = H(t):

$$R|_{z=H(t)} = R_0 + \varepsilon R^{(1)}|_{z=H_0} + \varepsilon^2 \left( R^{(2)}|_{z=H_0} + H_0 \sin(\omega t) \frac{\partial R^{(1)}}{\partial z} \Big|_{z=H_0} \right) + \cdots,$$
(A2)

$$\int_{0}^{H(t)} R^{2} dz = R_{0}^{2} H_{0} + \varepsilon \left( \int_{0}^{H_{0}} 2R_{0} R^{(1)} dz + R_{0}^{2} H_{0} \sin(\omega t) \right)$$

$$+ \varepsilon^{2} \left( \int_{0}^{H_{0}} [2R_{0} R^{(2)} + (R^{(1)})^{2}] dz + 2R_{0} R^{(1)}|_{z=H_{0}} H_{0} \sin(\omega t) \right) + \cdots,$$
(A3)

where we have substituted  $H(t) = H_0[1 + \varepsilon \sin(\omega t)]$ . Equations (A2)-(A3) enable transfer of the boundary conditions from the moving boundary at z = H(t) to the fixed boundary at  $z = H_0$ .

We will now systematically derive perturbative corrections to the cylinder solution for small strains. Inserting equations (A1)-(A3) into (16)-(19) and collecting terms of  $O(\varepsilon)$  gives,

$$\frac{\partial^2 R^{(1)}}{\partial z^2} + \frac{R^{(1)}}{R_0^2} = -\frac{p^{(1)}}{\gamma},\tag{A4}$$

at 
$$z = 0$$
,  $H_0$ :  $R^{(1)} = 0$ , (A5)

$$\int_0^{H_0} 2R_0 R^{(1)} dz = -R_0^2 H_0 \sin(\omega t). \tag{A6}$$

These equations govern the radius  $R^{(1)}(z,t)$  and pressure  $p^{(1)}(t)$ . Integrating equation (A4) and applying the two-point boundary conditions (A5) yields the following solution for the radius:

$$R^{(1)}(z,t) = \frac{R_0^2}{\gamma} \left[ \cos\left(\frac{z}{R_0}\right) + \frac{\sin\Lambda}{\cos\Lambda} \sin\left(\frac{z}{R_0}\right) - 1 \right] p^{(1)},$$

$$\approx \frac{2R_0^2}{\gamma} \Lambda^2 \frac{z}{H_0} \left(1 - \frac{z}{H_0}\right) p^{(1)}, \tag{A7}$$

where we have substituted  $\Lambda = H_0/(2R_0)$  and approximated the result for  $\Lambda^2 \ll 1$ . Inserting equation (A7) into (A6) then yields the solution for the pressure:

$$p^{(1)}(t) = -\frac{\gamma}{2R_0} \left( \frac{\Lambda \cos \Lambda}{\sin \Lambda - \Lambda \cos \Lambda} \right) \sin(\omega t)$$

$$\approx -\frac{3\gamma}{2R_0} \left( \frac{1}{\Lambda^2} - \frac{2}{5} \right) \sin(\omega t). \tag{A8}$$

To compute the force, we expand equation (18) up to  $O(\varepsilon)$  and insert (A8) for the pressure:

$$F^{(1)}(t) = -\pi R_0^2 p^{(1)}$$

$$= \frac{\pi \gamma R_0}{2} \left( \frac{\Lambda \cos \Lambda}{\sin \Lambda - \Lambda \cos \Lambda} \right) \sin(\omega t)$$

$$\approx \frac{3\pi \gamma R_0}{2} \left( \frac{1}{\Lambda^2} - \frac{2}{5} \right) \sin(\omega t). \tag{A9}$$

Note that the error in the approximation made in the last line is of  $O(\Lambda^2)$  and typically negligible.

Next, we consider the  $O(\varepsilon^2)$  problem. From the  $O(\varepsilon^2)$  terms in equations (16)-(19b), we derive the following boundary-value problem for the radius  $R^{(2)}(z,t)$  and pressure  $p^{(2)}(t)$ :

$$\frac{\partial^2 R^{(2)}}{\partial z^2} + \frac{R^{(2)}}{R_0^2} = -\frac{p^{(2)}}{\gamma} - \frac{1}{R_0} \left[ \frac{1}{2} \left( \frac{\partial R^{(1)}}{\partial z} \right)^2 - \frac{(R^{(1)})^2}{R_0^2} \right],\tag{A10}$$

at 
$$z = 0$$
,  $H_0$ :  $R^{(2)} = -H_0 \sin(\omega t) \frac{\partial R^{(1)}}{\partial z}$ , (A11)

$$\int_0^{H_0} [2R_0 R^{(2)} + (R^{(1)})^2] dz = -2R_0 R^{(1)}|_{z=H_0} H_0 \sin(\omega t).$$
(A12)

The force  $F^{(2)}(t)$  is then obtained by expanding equation (18) up to  $O(\varepsilon^2)$ :

$$F^{(2)}(t) = -\pi \gamma R_0 \left[ \frac{R_0 p^{(2)} + 2R^{(1)}|_{z=0} p^{(1)}}{\gamma} + \left( \frac{\partial R^{(1)}}{\partial z} \right)^2 \bigg|_{z=0} \right]. \tag{A13}$$

Unsurprisingly, the solution of the second-order problem is far more laborious than the first. However, the procedure is essentially unchanged from before. We shall simply quote the  $O(\varepsilon^2)$  correction for the force, which is of principal interest:

$$F^{(2)}(t) = -\frac{\pi \gamma R_0}{32} \left( \frac{27\Lambda^2}{(\sin \Lambda - \Lambda \cos \Lambda)^2} - \frac{\Lambda^2 [\sin (3\Lambda) - 3\Lambda \cos (3\Lambda)]}{(\sin \Lambda - \Lambda \cos \Lambda)^3} \right) \sin^2 (\omega t)$$

$$\approx -\frac{243\pi \gamma R_0}{40} \left( \frac{1}{\Lambda^2} - \frac{2}{35} \right) \sin^2 (\omega t). \tag{A14}$$

This procedure can be continued to obtain higher-order corrections; we have computed up to the  $O(\varepsilon^4)$  term. The final result for the dimensionless force  $\mathscr{F}(\tau) = F(t)/(\pi \gamma R_0)$  is given in Eq. (21).

- <sup>1</sup>J. Engmann, C. Servais, and A. S. Burbidge, "Squeeze flow theory and applications to rheometry: A review," J. Non-Newtonian Fluid Mech. **132**, 1–27 (2005).
- <sup>2</sup>S. L. Wingstrand, N. J. Alvarez, O. Hassager, and J. M. Dealy, "Oscillatory squeeze flow for the study of linear viscoelastic behavior," J. Rheol. **60**, 407–418 (2016).
- <sup>3</sup>D. Konigsberg, T. M. Nicholson, P. J. Halley, T. J. Kealy, and P. K. Bhattacharjee, "Online process rheometry using oscillatory squeeze flow," Appl. Rheol. **23**, 1–10 (2013).
- <sup>4</sup>K. J. Zwick, P. S. Ayyaswamy, and I. M. Cohen, "Oscillatory enhancement of the squeezing flow of yield stress fluids: A novel experimental result," J. Fluid Mech. **339**, 77–87 (1997).
- <sup>5</sup>K. H. Ahn, T. M. Nicholson, and P. J. Halley, "Technical note: Correcting for shear strain in an oscillatory squeeze flow rheometer," Rheol. Acta **53**, 103–107 (2014).
- <sup>6</sup>S. L. Wingstrand, N. J. Alvarez, and O. Hassager, "Linear viscoelastic characterization from filament stretching rheometry," in 10th Annual European Rheology Conference: Golden Jubilee Meeting of Groupe Français de Rhéologie (2015).
- <sup>7</sup>B. Debbaut and K. Thomas, "Simulation and analysis of oscillatory squeeze flow," J. Nonnewton. Fluid Mech. **124**, 77–91 (2004).
- <sup>8</sup>D. Bell, D. M. Binding, and K. Walters, "The oscillatory squeeze flow rheometer: comprehensive theory and a new experimental facility," Rheol. Acta 46, 111–121 (2006).
- <sup>9</sup>S. Gaudet, G. H. McKinley, and H. A. Stone, "Extensional deformation of Newtonian liquid bridges," Phys. Fluids 8, 2568–2579 (1996).
- <sup>10</sup>S. Gaudet and G. H. McKinley, "Extensional deformation of non-Newtonian liquid bridges," Comp. Mech. 21, 461–476 (1998).
- <sup>11</sup>M. Yao, G. H. McKinley, and B. Debbaut, "Extensional deformation, stress relaxation and necking failure of viscoelastic filaments," J. Non-Newtonian Fluid Mech. 79, 469–501 (1998).
- <sup>12</sup>T. Sridhar, V. Tirtaatmadja, D. A. Nguyen, and R. K. Gupta, "Measurement of extensional viscosity of polymer solutions," J. Non-Newtonian Fluid Mech. 40, 271–280 (1991).
- <sup>13</sup>S. H. Spiegelberg and G. H. McKinley, "Stress relaxation and elastic decohesion of viscoelastic polymer solutions in extensional flow," J. Non-Newtonian Fluid Mech. 67, 49–76 (1996).
- <sup>14</sup>H. K. Rasmussen and O. Hassager, "The role of surface tension on the elastic decohesion of polymeric filaments," J. Rheol. 45, 527–537 (2001).
- <sup>15</sup>J. F. Hutton, "Fracture and secondary flow of elastic liquids," Rheol. Acta 8, 54–59 (1969).
- <sup>16</sup>R. I. Tanner and M. Keentok, "Shear fracture in cone-plate rheometry," J. Rheol. 27, 47–57 (1998).
- <sup>17</sup>M. T. Johnston and R. J. Ewoldt, "Precision rheometry: Surface tension effects on low-torque measurements in rotational rheometers," J. Rheol. **57**, 1515–1532 (2013).
- <sup>18</sup>E. J. Hemingway, H. Kusumaatmaja, and S. M. Fielding, "Edge fracture in complex fluids," Phys. Rev. Lett. 119, 028006 (2017).

- <sup>19</sup>R. D. Gillette and D. C. Dyson, "Stability of fluid interfaces of revolution between equal solid circular plates," Chem. Eng. J. 2, 44–54 (1971).
- <sup>20</sup>S. R. Coriell, S. C. Hardy, and M. R. Cordes, "Stability of liquid zones," J. Colloid Interface Sci. 60, 126–136 (1977).
- <sup>21</sup>D. H. Michael, "Meniscus stability," Ann. Rev. Fluid Mech. **13**, 189–215 (1981).
- <sup>22</sup>D. Weihs, "Stability of a capillary jet with linearly increasing axial velocity (with application to shaped charges)," J. Fluid Mech. 155, 289–307 (1985).
- <sup>23</sup>M. J. Russo and P. H. Steen, "Instability of rotund capillary bridges to general disturbances: Experiment and theory," J. Colloid Interface Sci. 113, 154–163 (1986).
- <sup>24</sup>N. A. Bezdenejnykh, J. Meseguer, and J. M. Perales, "Experimental analysis of stability limits of capillary liquid bridges," Phys. Fluids A 4, 677–680 (1992).
- <sup>25</sup>L. A. Slobozhanin and J. M. Perales, "Stability of liquid bridges between equal disks in an axial gravity field," Phys. Fluids A 5, 1305–1314 (1993).
- <sup>26</sup>J. Meseguer, L. A. Slobozhanin, and J. M. Perales, "A review on the stability of liquid bridges," Adv. Sp. Res. 16, 5–14 (1995).
- <sup>27</sup>B. J. Lowry and P. H. Steen, "Capillary surfaces: stability from families of equilibria with application to the liquid bridge," Proc. - R. Soc. London, A 449, 411–439 (1995).
- <sup>28</sup>G. Domokos, I. Szeberényi, and P. H. Steen, "Simultaneously Resolved Bifurcation Diagrams: A Novel Global Approach Applied to Liquid Figures of Equilibrium," J. Comput. Phys. **159**, 38–57 (2000).
- <sup>29</sup>M. Gómez, I. E. Parra, and J. M. Perales, "Mechanical imperfections effect on the minimum volume stability limit of liquid bridges," Phys. Fluids 14, 2029–2042 (2002).
- <sup>30</sup>H. Cooray, H. E. Huppert, and J. A. Neufeld, "Maximal liquid bridges between horizontal cylinders," Proc. R. Soc. A Math. Phys. Eng. Sci. 472 (2016), 10.1098/rspa.2016.0233.
- <sup>31</sup>M. Haynes, E. J. Vega, M. A. Herrada, E. S. Benilov, and J. M. Montanero, "Stabilization of axisymmetric liquid bridges through vibration-induced pressure fields," J. Colloid Interface Sci. 513, 409–417 (2018).
- <sup>32</sup>Y. C. Liao, H. J. Subramani, E. I. Franses, and O. A. Basaran, "Effects of soluble surfactants on the deformation and breakup of stretching liquid bridges," Langmuir 20, 9926–9930 (2004).
- <sup>33</sup>P. M. Kamat, B. W. Wagoner, S. S. Thete, and O. A. Basaran, "Role of Marangoni stress during breakup of surfactant-covered liquid threads: Reduced rates of thinning and microthread cascades," Phys. Rev. Fluids 3 (2018), 10.1103/PhysRevFluids.3.043602.
- <sup>34</sup>P. Hoyer and V. Alvarado, "Stability of liquid bridges with elastic interface," RSC Adv. 7, 49344–49352 (2017).
- <sup>35</sup>H. Chen, A. Amirfazli, and T. Tang, "Modeling liquid bridge between surfaces with contact angle hysteresis," Langmuir 29, 3310–3319 (2013).
- <sup>36</sup>O. Pitois, P. Moucheront, and X. Chateau, "Liquid bridge between two moving spheres: an experimental study of viscosity effects," J. Colloid Interface Sci. 231, 26–31 (2000).
- <sup>37</sup>S. L. Anna and G. H. McKinley, "Effect of a controlled pre-deformation history on extensional viscosity of dilute polymer solutions," Rheol. Acta 47, 841–859 (2008).
- <sup>38</sup>J. M. Montanero, G. Cabezas, J. Acero, and J. M. Perales, "Theoretical and experimental analysis of the equilibrium contours of liquid bridges of arbitrary shape," Phys. Fluids 14, 682–693 (2002).
- <sup>39</sup>J. M. Montanero, "On the experimental analysis of linear dynamics of slender axisymmetric liquid bridges," Microgravity Sci. Technol. 15, 3–11 (2004).
- <sup>40</sup>E. J. Vega and J. M. Montanero, "Damping of linear oscillations in axisymmetric liquid bridges," Phys. Fluids 21 (2009), 10.1063/1.3216566.
- <sup>41</sup>J. M. Montanero and A. Ponce-Torres, "Review on the dynamics of isothermal liquid bridges," Appl. Mech. Rev. 72, 1–29 (2020).
- <sup>42</sup>A. Ponce-Torres, E. J. Vega, and J. M. Montanero, "Effects of surface-active impurities on the liquid bridge dynamics," Exp. Fluids **57**, 67–78 (2016).
- <sup>43</sup>A. Ponce-Torres, M. A. Herrada, J. M. Montanero, and J. M. Vega, "Linear and nonlinear dynamics of an insoluble surfactant-laden liquid bridge," Phys. Fluids 28, 112103 (2016).
- <sup>44</sup>M. A. Herrada, J. M. Montanero, and J. M. Vega, "The effect of surface shear viscosity on the damping of oscillations in millimetric liquid bridges," Phys. Fluids 23, 082102 (2011).
- <sup>45</sup>J. B. Valsamis, M. Mastrangeli, and P. L. Lambert, "Vertical excitation of

- axisymmetric liquid bridges," Eur. J. Mech. B/Fluids. 38, 47-57 (2013).
- <sup>46</sup>R. J. Larsen, M. D. Dickey, G. M. Whitesides, and D. A. Weitz, "Viscoelastic properties of oxide-coated liquid metals," J. Rheol. **53**, 1305–1326 (2009).
- <sup>47</sup>Y.-C. Liao, H. J. Subramani, E. I. Franses, and O. A. Basaran, "Effects of Soluble Surfactants on the Deformation and Breakup of Stretching Liquid Bridges," Langmuir 20, 9926–9930 (2004).
- <sup>48</sup>J. Stefan, "Versuche über die scheinbare Adhäsion," Sitz. Kais. Akad. Wiss Math. Nat. Wien 69, 713–735 (1874).
- <sup>49</sup>N. Phan-Thien, "Small strain oscillatory squeeze film flow of simple fluids," J. Austral. Math. Soc. **22**, 22–27 (1980).
- <sup>50</sup>N. Phan Thien, F. Sugeng, and R. I. Tanner, "The squeeze-film flow of a viscoelastic fluid," J. Non-Newtonian Fluid Mech. 24, 97–119 (1987).
- <sup>51</sup>S. H. Spiegelberg, D. C. Ables, and G. H. McKinley, "The role of endeffects on measurements of extensional viscosity in filament stretching rheometers," J. Non-Newtonian Fluid Mech. **64**, 229–267 (1996).
- <sup>52</sup>A. C. Pipkin, *Lectures on Viscoelasticity Theory*, 2nd ed. (Springer, 1986).
- <sup>53</sup>J. S. Field, M. V. Swain, and N. Phan-Thien, "An experimental investigation of the use of random squeezing to determine the complex modulus of viscoelastic fluids," J. Non-Newtonian Fluid Mech. 65, 177–194 (1996).
- <sup>54</sup>J. A. Tichy and W. O. Winer, "Inertial considerations in parallel circular squeeze film bearings," ASME J. Lub. Tech. **92**, 588–592 (1970).
- <sup>55</sup>L. G. Leal, Advanced transport phenomena: fluid mechanics and convective transport processes (Cambridge University Press, 2007).

- <sup>56</sup>R. I. Tanner, "Some illustrative problems in the flow of viscoelastic non-Newtonian lubricants," ASLE Transactions 8, 179–183 (1965).
- <sup>57</sup>G. Williams and R. I. Tanner, "Effects of combined shearing and stretching in viscoelastic lubrication," J. Lub. Tech. 92, 216–219 (1970).
- <sup>58</sup>P. A. Kralchevsky and K. Nagayama, "Capillary bridges and capillary-bridge forces," in *Studies in Interface Science*, Vol. 10 (Elsevier, 2001) pp. 469–502.
- <sup>59</sup>H. Kusumaatmaja and R. Lipowsky, "Equilibrium morphologies and effective spring constants of capillary bridges," Langmuir 26, 18734–18741 (2010)
- <sup>60</sup>M. van Dyke, "Analysis and improvement of perturbation series," Q. J. Mechanics Appl. Math. 27, 423–450 (1974).
- <sup>61</sup>D. W. van Krevelen and K. Te Nijenhuis, *Properties of Polymers*, 4th ed. (Elsevier, 2009).
- <sup>62</sup>A. Sanz and J. L. Diez, "Non-Axisymmetric oscillations of liquid bridges," J. Fluid Mech. **205**, 503–521 (1989).
- <sup>63</sup>N. J. Alvarez, L. M. Walker, and S. L. Anna, "Diffusion-limited adsorption to a spherical geometry: the impact of curvature and competitive time scales." Phys. Rev. E **82**, 011604 (2010).
- <sup>64</sup>N. J. Alvarez, L. M. Walker, and S. L. Anna, "A microtensiometer to probe the effect of radius of curvature on surfactant transport to a spherical interface," Langmuir 26, 13310–13319 (2010).